ROBUST FRAME BASED X-RAY CT RECONSTRUCTION[*]

Jia Li

Department of Mathematical Science, Rensselaer Polytechnic Institute, Troy, NY 12180, USA
Email: lij25@rpi.edu

Chuang Miao

Department of Biomedical Engineering, Wake Forest University Health Sciences, Winston-Salem, NC,
27157, USA; and Biomedical Imaging Division, VT-WFU School of Biomedical Engineering and
Sciences, Wake Forest University Health Sciences, Winston-Salem, NC, 27157, USA
Email: cmiaowfu@gmail.com

Zuowei Shen

Department of Mathematics, National University of Singapore, Singapore 119076
Email: matzuows@nus.edu.sg

Ge Wang

Biomedical Imaging Cluster, Department of Biomedical Engineering, Rensselaer Polytechnic Institute
Troy, NY 12180, USA
Email: wangg6@rpi.edu

Hengyong Yu

Department of Electrical and Computer Engineering, University of Massachusetts Lowell, MA 01854,
USA
Email: hengyong-yu@ieee.org

Abstract

As X-ray computed tomography (CT) is widely used in diagnosis and radiotherapy, it is important to reduce the radiation dose as low as reasonably achievable. For this purpose, one may use the TV based methods or wavelet frame based methods to reconstruct high quality images from reduced number of projections. Furthermore, by using the interior tomography scheme which only illuminates a region-of-interest (ROI), one can save more radiation dose. In this paper, a robust wavelet frame regularization based model is proposed for both global reconstruction and interior tomography. The model can help to reduce the errors caused by mismatch of the huge sparse projection matrix. A three-system decomposition scheme is applied to decompose the reconstructed images into three different parts: cartoon, artifacts and noise. Therefore, by discarding the estimated artifacts and noise parts, the reconstructed images can be obtained with less noise and artifacts. Similar to other frame based image restoration models, the model can be efficiently solved by the split Bregman algorithm. Numerical simulations show that the proposed model outperforms the FBP and SART+TV methods in terms of preservation of sharp edges, mean structural similarity (SSIM), contrast-to-noise ratio, relative error and correlations. For example, for real sheep lung reconstruction, the proposed method can reach the mean structural similarity as high as 0.75 using only 100 projections while the FBP and the SART+TV methods need more than 200 projections. Additionally, the proposed robust method is applicable for interior and exterior tomography with better performance compared to the FBP and the SART+TV methods.

Mathematics subject classification: 15A15, 15A09, 15A23.
Key words: Computed tomography, Wavelet frame, Split Bregman algorithm.

1. Introduction

In the clinical applications of X-ray Computed Tomography (CT), it is important to reduce the X-ray dose while preserving the quality of CT image reconstruction. The X-ray CT reconstruction problem can be essentially represented as a linear inverse problem:

$$Pu = f, \tag{1.1}$$

where $P \in \mathbb{R}^{m \times n}$ is a measurement matrix representing the collection of discrete line integrations at different projection angles and along different beamlets, $u \in \mathbb{R}^n$ is a vector rearranging from a 2 dimensional image and $f \in \mathbb{R}^m$ is the measurement of u. The CT reconstruction is to recover the image u from a given P and f [26]. Because P is determined by the direction and location of the available beamlets, the matrix P can be approximately generated by the information from the X-ray projection geometry. However, due to the mechanical error, beam hardening, finite source and detector cell effects, and other factors, the actual measurement f does not equal to Pu. In fact, the reconstruction problem can be redefined as:

$$(P + P_\delta)u = f + \epsilon, \tag{1.2}$$

where P_δ represents the model mismatch part of the projection matrix P caused by all the possible factors, ϵ is the additive noise. A difficulty of solving problems (1.1) and (1.2) is that the linear system will become ill-posed if we decrease the projection number or detector cell number for dose reduction. For example, the interior tomography [33, 34] and exterior tomography are to reconstruct a region of interest (ROI) only from the measured X-rays passing through this ROI and aided by some prior information. Appropriate application of interior and exterior tomography can reduce the X-ray dose to the patients. Fig. 1.1 shows the sinogram for full CT imaging, interior tomography and exterior tomography, the ROI correspond to the pixels whose projection lines in all angles are available. Each sinogram can be regarded as the reshape of input f, where the columns represent different projection views and the rows represent different projection lines in each view. Therefore, the interior and exterior tomography can be regarded as special CT reconstruction with incomplete Radon domain measurement.

As a result, in (1.2), the matrices P and P_δ have much smaller number of rows comparing to the number of the columns. It is difficult to determine the most appropriate u from infinitely many solutions of the problem (1.1) and (1.2). Although the current state-of-the-art clinical CT scanner does not support a scan with reduced projections, image reconstruction from few-view projections has been a hot topic. The recent development of carbon-nano tube based X-ray source make it possible for fast switch for the acquisition of sparse projections. Similar to the flush gate in a camera, it is possible to build a special flush gate and install it in front of the conventional X-ray source to control the overexposure of X-ray.

Although there are some classical methods available, such as the filtered back projection (FBP) type methods [11,16,24,25] and the algebraic reconstruction techniques (ART) [19], these methods usually suffer from artifacts especially when the number of projection is insufficient. To reconstruct the image u from the noisy measurement, some differential operator based regularization methods have been introduced. The total variation (TV) based method is one of the well-known regularization methods and has been proven by its application in various fields such as signal recovery and image processing [5, 28]. The TV-based model, sometimes called as Rudin-Osher-Fatemi (ROF) model [28], has been applied to 3D X-ray cone beam CT reconstruction [30, 31] and 2D CT reconstruction [23]. In the compressed sensing framework,

it can be found that a 2D interior region-of-interest (ROI) can be exactly reconstructed by minimizing the TV if the image on the ROI is piecewise constant [20, 34, 35]. The canonical form of TV-based CT reconstruction model is defined as:

$$\min_u \frac{1}{2}\|Pu - f\|_2^2 + \lambda\|\nabla u\|_1. \tag{1.3}$$

where P, u and f are identical to those in (1.1), ∇ is the discretization of 2D gradient operator and λ is a parameter to balance the fidelity and regularity terms in the minimization problem (1.3).

1.1. Existing wavelet frame based X-ray CT reconstruction

The frame based approaches have similar form of variational methods such as TV-based model (1.3). It has been shown that the analysis based approach can be regarded as a finite difference approximation of a certain type of general variational model, and such approximation will be exact when the image resolution goes to infinity [2]. On the other hand, the discretizations provided by wavelet frames were shown always to be superior than the standard discretizations for the TV-based model (1.3) [2–4, 6, 8, 14]. This is due to the multiresolution structure and redundancy of wavelet frames, which enable wavelet frame based models to adaptively choose a proper differential operators in different regions for a given image according to the order of the singularity (non-smooth part) of the underlying solutions. More details of the definition of wavelet frames can be seen in Section 2.1.

The general wavelet frame based image restoration model can be written as:

$$\alpha^* = \arg\min_\alpha \left\{ \frac{1}{2}\|PW^T\alpha - f\|_2^2 + \frac{\kappa}{2}\|(I - WW^T)\alpha\|_2^2 + \|\mathrm{diag}(\lambda)\alpha\|_1 \right\}. \tag{1.4}$$

where α is the wavelet frame coefficients of estimated object image, W represents the wavelet transform and $u = W^T\alpha$, $u^* = W^T\alpha^*$ is the reconstructed object image for this model. Note that the wavelet transform W satisfies $W^TW = I$ but $WW^T \neq I$ therefore the second term measures the distance between α and the range space of W. When $\kappa = 0$, the model (1.4) is called the synthesis based approach which emphasize the sparsity of frame coefficients. When $\kappa = \infty$, it is equivalent to add the constraint $\|(I - WW^T)\alpha\|_2^2 = 0$ or $\alpha = Wu$ to model (1.4). In this case, the model (1.4) is therefore called the analysis based approach which emphasize the regularity. When $0 < \kappa < \infty$, the model (1.4) becomes a balanced approach between the previous two approaches.

The wavelet frame has been first applied to the X-ray CT reconstruction in 2010 [22], in which the model is essentially balanced approach methods [6, 7]. The analysis approach outperforms the TV-based model and balanced approach model in terms of relative error and correlations. The analysis approach were first proposed in 2012 [13] where the isotropic wavelet frame [2] and Radon domain inpainting were also proposed. The isotropic wavelet frame treats the singularity in different direction equally and such frame is extremely good at removing the artifacts during CT reconstruction. The Radon domain inpainting mechanism regards the measurement as a $N_d \times N_p$ 2D image and inpaints it to $N_d \times 2N_p$ image, where N_d is the number of beamlets for each view and N_p is the number of views. The inpainted result would include more information in Radon domain and can generate better reconstruction result although the inpainted information is not 100% accurate. The model [13] attempted to alternatively updated the inpainted measurement and the CT reconstruction object image to search for the
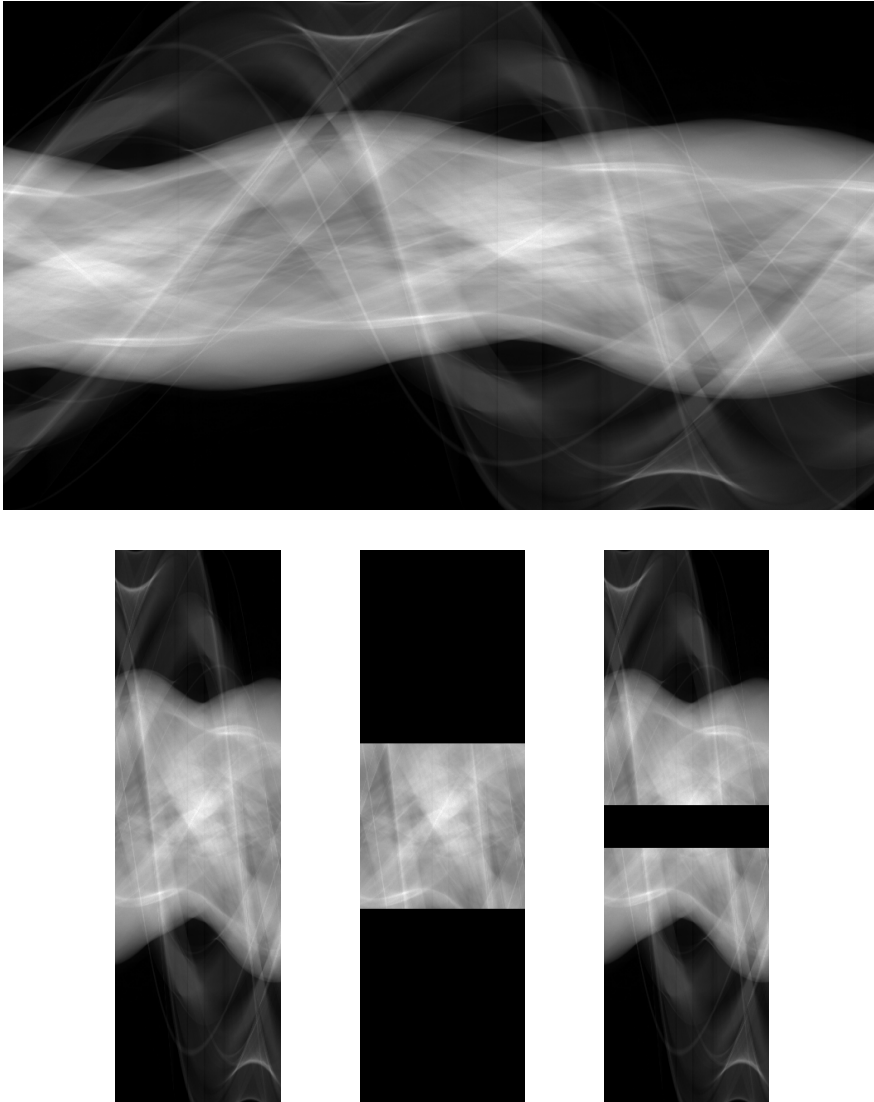
Fig. 1.1. The sinogram for different type of CT reconstruction. The first row shows the original measurement of CT projection of a sheep lung by a SIEMENS scanncer with 1160 views. The second row from left to right shows: 200 views sampled from the original measurement for full CT imaging, truncated sinogram in each view for interior tomography (only middle 30% projection lines are available), tuncated sinogram in each view for exterior tomography (middle 7.5% projection lines is not available).

result with less relative error and more correlations. The Radon domain inpainting can help to reconstruct more details with several times of computational cost. Since the Radon domain inpainting makes the algorithm more complicated and greatly increase the computational and memory costs, here the general analysis based model without Radon domain inpainting can be stated as follows:

$$\min_u \frac{1}{2}\|Pu - f\|_2^2 + \lambda\|Wu\|_{1,p}, \tag{1.5}$$

where the norm $\| \cdot \|_{1,p}$ is defined as

$$\|Wu\|_{1,p} = \left\| \sum_{l=1}^{L} (\sum_{(i,j) \neq (0,0)} |W_{l,i,j}u|^p)^{\frac{1}{p}} \right\|_1, \quad p = 1, 2. \tag{1.6}$$

In (1.6), $W_{l,i,j}$ is the wavelet frame decomposition operator with the level l and the framelet bands (i,j). In particular, $(i,j) \in \{0,1,2\} \times \{0,1,2\}$ for 2 dimensional linear B-spline wavelet tight frames and only $(i,j) = (0,0)$ represents the low pass frame band. When $p = 1$, the norm $\| \cdot \|_{1,1}$ is referred to as the *anisotropic* ℓ_1-norm of the frame coefficients, which is the standard ℓ_1-norm used for frame based image restoration problems. When $p = 2$, the norm $\| \cdot \|_{1,2}$ is referred to as the *isotropic* ℓ_1-norm of the frame coefficients. In [13] it has been shown that the isotropic ℓ_1-norm regularization performs better, which coincides with the theoretical analysis in [2].

In practice, however, there are still two problems that have not been solved by the wavelet frame based model with Radon domain inpainting [13]. First, the projection matrix P does not match the real measurements as stated in (1.2). The model (1.5) works extremely well if $P_\delta = 0$, but not so good if the P has a larger error. Second, for some high resolution imaging objects, there are some tiny structures which may be recognized as noise or artifacts by (1.5). Those motivate us to generate a new method to keep the tiny singularity and remove the noise and artifacts simultaneously.

1.2. The goal and structure of this paper

In this paper a robust isotropic wavelet frame [2, 9, 10, 27] based CT reconstruction model will be proposed. This model is robust to the error of the matrix P and can preserve more tiny features during the process of suppress noise and artifacts. The rest of this paper is organized as follows. Section 2 is devoted to introduce the wavelet frames, design the CT reconstruction model and algorithm. The numerical results for both simulated phantom and real sheep lung reconstruction are presented in Section 3. Finally, the major results and conclusions will be summarized in Section 4.

2. Method

To obtain better CT reconstruction results compared to the FBP and the SART+TV method, it is necessary to introduce new regularization scheme such as the wavelet tight frame regularization. Firstly in this section, the definition and some basic concepts of the wavelet tight frame will be briefly provided. Then, a three-system method with wavelet frame regularization will be proposed to solve the CT reconstruction with an inaccurate matrix P. At last, an alternative minimization algorithm based on the split Bregman algorithm will be presented to solve the proposed frame based CT reconstruction problem.

2.1. Wavelet tight frames

In this subsection, the concept of wavelet tight frames and its framelets will be briefly introduced. For more information, interested readers can refer to the related materials [9, 10, 14, 27, 29] for theories and survey.

A countable set $X \subset L_2(\mathbb{R})$ is called a tight frame of $L_2(\mathbb{R})$ if

$$f = \sum_{h \in X} \langle f, h \rangle h \quad \forall f \in L_2(\mathbb{R}), \tag{2.1}$$

where $\langle \cdot, \cdot \rangle$ is the inner product of $L_2(\mathbb{R})$. Given a finite collection of functions $\Psi = \{\psi_1, \psi_2, ..., \psi_m\}$, define $X = \{\psi_{n,k,i} = 2^{n/2}\psi_i(2^n \cdot -k), 1 \leq i \leq m\}$. If X is a tight frame, then X is called a wavelet tight frame and Ψ is called wavelet. The multi-resolution analysis (MRA) based wavelet can be generated by the unitary extension principle (UEP) [27]. In this work, we will use the piecewise linear B-spline framelets [27]. Given a 1-dimensional framelet system for $L_2(\mathbb{R})$, the s-dimensional tight wavelet frame system for $L_2(\mathbb{R}^s)$ can be easily constructed by using tensor products of 1-dimensional framelets [9, 14].

In the discrete setting, a discrete image u is an s-dimensional array. The matrix W denotes fast tensor product framelet decomposition and use $W^\top$ to denote the fast reconstruction. Then by the unitary extension principle [27], we have $W^\top W = I$, i.e. $u = W^\top W u$ for any image u. The L-level framelet decomposition of u will be further defined as

$$Wu = \left\{ W_{l,i,j}u : 1 \leq l \leq L, (i,j) \in I_0 \right\},$$

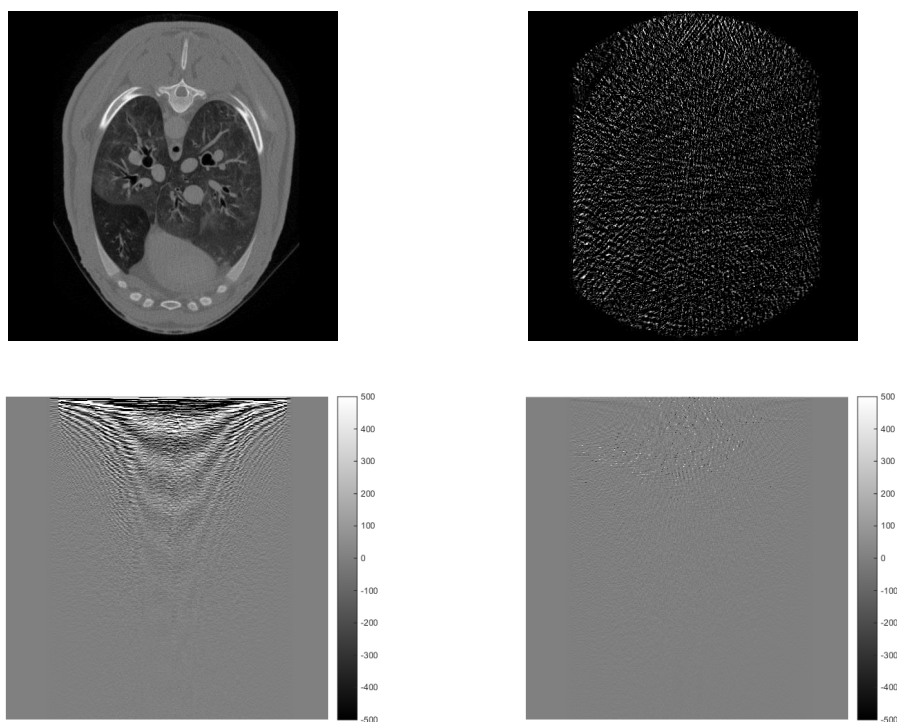where I_0 denotes the index set of all framelet bands.

Fig. 2.1. The discrete cosine transform (DCT) of the groundtruth image and artifacts generated by the FBP method with 100 projections. The first row from left to right show the "ground truth" from full measurement, and the artifacts generated by the FBP method with 100 projections. The second row show the corresponding DCT result with common color bar, which shows that the artifacts has sparse representation in DCT transform domain.

2.2. Robust wavelet frame model and algorithm

In this subsection, we will propose an wavelet frame based CT reconstruction method which is robust for inaccurate estimation of projection matrix P. The idea is to apply a three-system method [1, 15] to separate and treat different image parts by different regularization terms. In this paper, the image to be reconstructed can be decomposed to three parts: the information part we want to restore (or cartoon part), the artifacts generated by the machine error and insufficient measurement, and the noise part. Therefore, the three-system model can regularize the noise part with its sparsity in Radon domain, artifacts part in discrete cosine transform (DCT) domain, and information part in wavelet frame transform domain. Such an idea was partially illuminated from the robust image deblurring with inaccurate blur kernels [21], in which the inaccurate blur kernel is essentially the error of the linear operator from the image to its corresponding measurement. Fig. 2.1 shows that compared the cartoon part, the artifacts part has highly sparse representation in DCT transform domain.

Therefore, in this paper the error of P plays the same role as that of the blur kernels. Applying the form of analysis based approach and the three-system structure, the robust frame based model can be stated as:

$$\min_{u,a,n} \frac{1}{2}\|P(u+a)+n-f\|_2^2 + \lambda_1\|Wu\|_{1,2} + \lambda_2\|Da\|_1 + \lambda_3\|n\|_1. \qquad (2.2)$$

where f is the projection data from the detector, u is the reconstructed image, a represents the estimated artifacts caused by inaccurate P, and n stands for the additive impulse noise in Radon domain (See [12] for plugging ℓ_1 norm regularization for additive impulse noise). P is the anticipated projection matrix including totally N_p projections. The matrix $W = \{W_{l,i,j} : 1 \leq l \leq L, (i,j) \in \{0,1,2\} \times \{0,1,2\}, ij \neq 0\}$ is the 2D decomposition operator associated with the linear B-spline framelet system. For the wavelet systems, l represents the layer and i,j represent the different windows of the frame coefficient, where only $(i,j) = (0,0)$ stands for the lower-pass coefficient. The operator D represents the DCT transform. We assume the vector Da is sparse in the corresponding DCT transform domain and the noise vector n is itself sparse in the spatial domain. $\lambda_1, \lambda_2, \lambda_3$ are parameters to balance the regularization of the three systems. Because the model (2.2) is convex for all its variables u, a and n, it can be alternatively optimized to simultaneously converge to the optimized solution [32]. In particular, the value of u is the object image.

To solve the problem (2.2), an alternative optimization algorithm is proposed. The outline of the algorithm is summarized in Algorithm 2.1, where the variable ϵ is a given error tolerance.

The Step 3 in Algorithm 2.1 can be easily solved by a simple one-time soft thresholding operation. In particular, if we define the soft thresholding operator $\mathcal{T}$ as:

$$\mathcal{T}_t(v)_i := \frac{\max(|v_i|-t,0)}{|v_i|} \cdot v_i, \qquad (2.3)$$

the Step 3 can be reinterpreted as $n^{k+1} := \mathcal{T}_{\lambda_3}(f - P(u^{k+1} + a^{k+1}))$. To solve the Steps 1 and 2 fast and accurately, the split Bregman algorithm is necessary to be applied here. The split Bregman algorithm was initially stated out in [18] which was shown to be convergent and powerful [18, 39] when it is applied to various variational models for image restoration, e.g., ROF [28] and nonlocal variational models [17]. More convergence analysis of the split Bregman was given in 2009 [4]. The the split Bregman algorithm to CT reconstruction is also applied in the isotropic wavelet frame based CT reconstruction method with Radon domain inpainting [13]. Therefore, a detail algorithm to solve (2.2) is given in Algorithm 2.2.

Algorithm 2.1 Outline of the alternative optimization algorithm to solve (2.2)

Step 0. Set the initial values such that $u^{-1} = -1, u^0 = 0, a^0 = 0, n^0 = 0, k = 0$.

while the stopping criteria ($k \geq 1$ and $\|u^k - u^{k-1}\|_2^2 \leq \epsilon$) are not met **do**

Step 1. Solve

$$u^{k+1} := \min_u \frac{1}{2} \|P(u + a^k) + n^k - f\|_2^2 + \lambda_1 \|Wu\|_{1,2}.$$

Step 2. Solve

$$a^{k+1} := \min_a \frac{1}{2} \|P(u^{k+1} + a) + n^k - f\|_2^2 + \lambda_2 \|Da\|_1.$$

Step 3. Solve

$$n^{k+1} := \min_n \frac{1}{2} \|P(u^{k+1} + a^{k+1}) + n - f\|_2^2 + \lambda_3 \|n\|_1.$$

Step 4. Let

$$k := k + 1.$$

end while

Algorithm 2.2 Detailed Algorithm 2.1

Step 0. Set the initial values such that $u^0 = u^{-1} = 0, d_u^0 = 0, b_u^0 = 0, a^0 = 0, d_a^0 = 0, b_a^0 = 0, n^0 = 0, k = 0$.

Step 1. Perform the following iterations until the stopping criteria ($k \geq 1$ and $\|u^k - u^{k-1}\|_2^2 \leq \epsilon$) are met.

$$
\begin{cases}
u^{k+1} := \arg\min_u \frac{1}{2}\|P(u + a^k) + n^k - f\|_2^2 \\
\qquad + \frac{\mu_1}{2}\|Wu - d_u^k + b_u^k\|_2^2 \\
\qquad = (P^\top P + \mu_1 W^\top W)^{-1}(P^\top(f - Pa^k - n^k) \\
\qquad + \mu_1 W^\top(d_u^k - b_u^k)) \\
d_u^{k+1} := \mathcal{T}'_{\lambda_1/\mu_1}(Wu^{k+1} - b_u^k) \\
b_u^{k+1} := b_u^k + (Wu^{k+1} - d_u^{k+1}) \\
a^{k+1} := \arg\min_a \frac{1}{2}\|P(u^{k+1} + a) + n^k - f\|_2^2 \\
\qquad + \frac{\mu_2}{2}\|Da - d_a^k + b_a^k\|_2^2 \\
\qquad = (P^\top P + \mu_2 D^\top D)^{-1}(P^\top(f - Pu^{k+1} - n^k) \\
\qquad + \mu_2 D^\top(d_a^k - b_a^k)) \\
d_a^{k+1} := \mathcal{T}_{\lambda_2/\mu_2}(Da^{k+1} - b_a^k) \\
b_a^{k+1} := b_a^k + (Da^{k+1} - d_a^{k+1}) \\
n^{k+1} := \mathcal{T}_{\lambda_3}(f - P(u^{k+1} + a^{k+1}))
\end{cases}
$$

where μ_1 and μ_2 are parameters for iteration and do not need to be rigorously chosen since the value will not affect the optimal solution of the model and the convergence of the algorithm. The thresholding operator $\mathcal{T}$ is defined by (2.3) and the operator $\mathcal{T}'$ is the isotropic thresholding operator defined as in (2.4).

$$(\mathcal{T}'_t(v))_{l,(i,j)} = \begin{cases} v_{l,(i,j)}, \text{ if } (i,j) = (0,0) \\ \frac{v_{l,(i,j)}}{R_l} \max(R_l - t, 0), \text{ if } (i,j) \neq (0,0) \end{cases} \tag{2.4}$$

with $R_l = (\sum_{(i,j) \neq (0,0)} |v_{l,(i,j)}|^2)^{\frac{1}{2}}$ where (i,j) represents for different high-pass frame windows and $(0,0)$ is the low-pass frame window. Note that $W^\top W = I$ and $D^\top D = I$ always hold. The conjugate gradient method can be used to solve the above linear systems for u^{k+1} and a^{k+1} in each iteration.

3. Numerical Results

In this section, the proposed robust frame based model (2.2) with three-system structure will be evaluated and compared to the filtered back projection (FBP) and the simultaneous algebraic reconstruction technique (SART) method with total variation (TV) regularization. For numerical simulations, firstly the modified Shepp-Logan phantom is chosen to simulate a human head. A typical SIEMENS fan-beam geometry is assumed, which includes 672 detector cells and 1160 projections for a full scan. Both the measurements with and without Poisson noise are considered. Poisson noise was simulated according to the physical imaging chain based method [36]. While the strength of Poisson noise is increased with respect to increase of the number of photons, the signal noise ratio is decreased. We downsampled the vector f using merely 75, 100 and 150 projections from the original 1160 projections. To simulate local projections for interior reconstruction, the middle 202 (30%) detector cells in each projection are extracted. Moreover, real projections of a sheep lung scanned by a SIEMENS scanner [37] is also employed in this paper. In all experiments of the CT reconstruction, all the parameters are fixed except λ_1 which is determined by the smoothness of the estimated reconstruction result. Comparing to the Shepp-Logan phantom, the real sheep lung has less flat regions and more tiny structures which can not be easily distinguished from the artifacts. Therefore, the optimal parameter λ_1 should be relatively small. For the proposed frame based method (2.2), we set $\lambda_1 = 4.0$ for the Shepp-Logan phantom reconstruction and $\lambda_1 = 0.01$ for the real sheep lung reconstruction. For other parameters, we always set $\lambda_2 = 0.05, \lambda_3 = 10$.

Besides the visual quality, the mean structural similarity (SSIM) [38] and contrast-to-noise ratio (CNR) are used to quantitatively evaluate the quality of the reconstructed results. The general form of the structural similarity can be defined as in (3.1). In practice, the mean SSIM is calculated by taking average of the SSIM values from different Gaussian window with $hsize = 11$ and $\sigma = 1.5$.

$$SSIM(x,y) = \frac{(2\mu_x\mu_y + c_1)(2\sigma_x\sigma_y + c_2)}{(\mu_x^2 + \mu_y^2 + c_1)(\sigma_x^2 + \sigma_y^2 + c_2)}, \tag{3.1}$$

where μ_x and μ_y are the average of the image patch x and y, respectively. σ_x and σ_y denote the variance of x and y. c_1 and c_2 are two constants to stabilize the division with weak denominator and their default settings are $c_1 = 0.01$ and $c_2 = 0.03$.

The CNR value is defined as the ratio between the intensity difference of two flat regions and the estimated noise standard deviation. The regions chosen for both the Shepp-Logan phantom and the real sheep lung are indicated by the circles in Fig. 3.1.
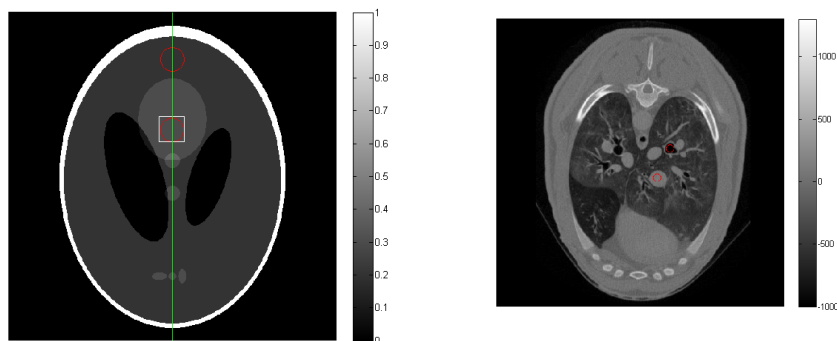

Fig. 3.1. The object images for numerical simulations. The left one is a modified Shepp-Logan phantom and the right one is a real sheep lung. The red circles indicates the regions for calculating the contrast-to-noise ratio (CNR). The white square indicates the magnified region of Fig. 3.5. The green lines are the positions of the profiles in Fig. 3.6.

Moreover, we also consider the relative error and correlation which are defined in (3.2) and (3.3) respectively.

$$err(u) = \frac{\|u - \tilde{u}\|_2}{\|\tilde{u}\|_2}, \tag{3.2}$$

$$corr(u) = \frac{(u - \bar{u})(\tilde{u} - \bar{\tilde{u}})}{\|u - \bar{u}\|_2 \|\tilde{u} - \bar{\tilde{u}}\|_2}, \tag{3.3}$$

where $\tilde{u}$ denotes the ground truth, $\bar{u}$ and $\bar{\tilde{u}}$ denote the mean values of u and $\tilde{u}$ respectively. For numerical simulations of the Shepp-Logan phantom, the ground truth is selected as the phantom image. For the real lung study, the FBP reconstruction result from 1160 projections is chosen as the ground truth.

Regarding to the computational time, we take the reconstruction of sheep lung (resolution 512×512) from 100 views as an example. Note that all the numerical simulations are executed via personal laptop with CPU Intel Core P8700 (two CPUs with frequency 2.53GHz) and memory 4GB. The FBP method needs 0.015s for each view and the total computational time about 1.5 seconds. The SART+TV method is an iterative method and the time consumption is 0.03s for each view and per iteration. The reconstruction is stopped after 250 and the total computational cost is 750 ($0.03 \times 100 \times 250$) seconds for the SART+TV method. The proposed frame based method is relatively complicated than other methods. For each iteration of the corresponding split Bregman algorithm, two linear systems need to be solved and each of them takes 50 iterations of conjugate gradient methods. Generally, it needs 42.2 seconds for one iteration of split Bregman algorithm. Fortunately, only 10 iterations of split Bregman algorithm is necessary to approach the solution therefore the total computational cost is about 422 seconds.

The reconstructed results are shown in Figs. 3.2–3.10. Figs. 3.2, 3.4–3.7 and 3.9 are for global reconstruction and the others are for interior tomography [33,34]. The quantitative anal-
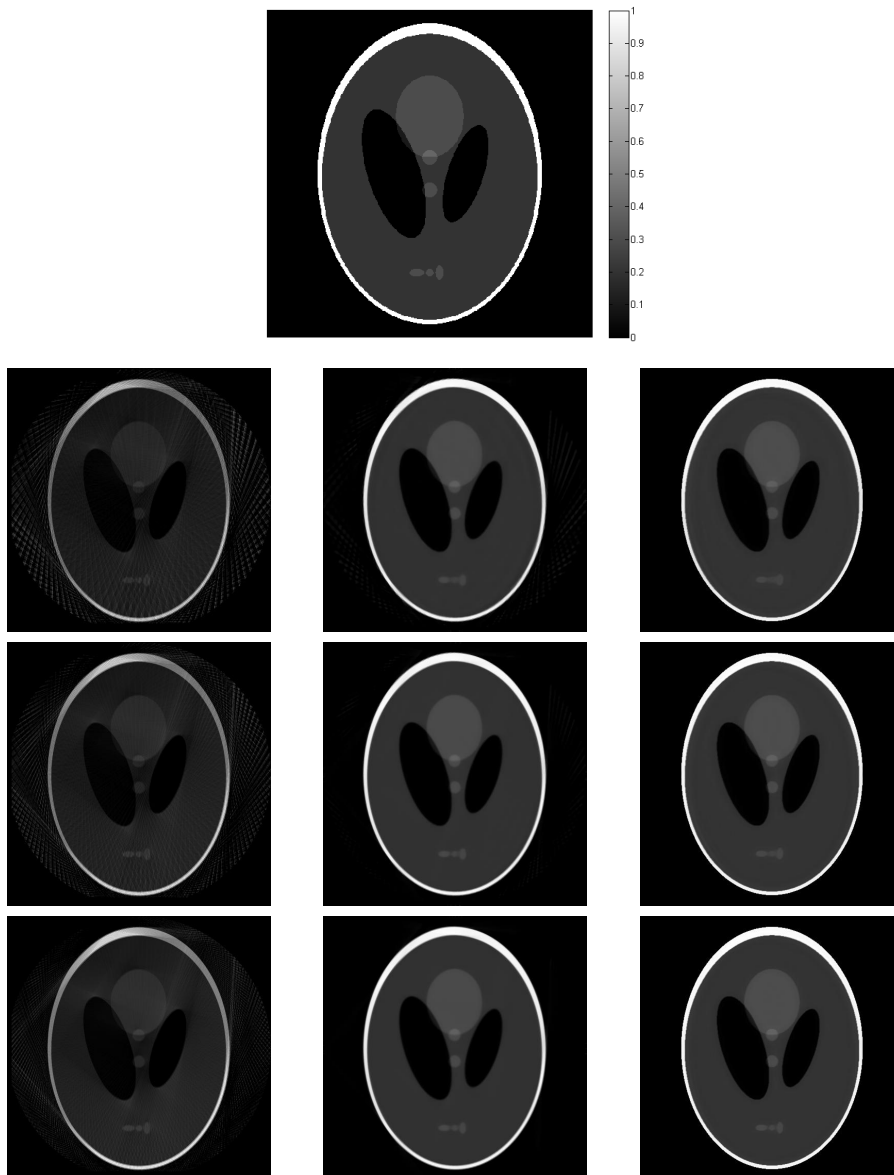
Fig. 3.2. The tomographic results (512 × 512) of the Shepp-Logan phantom reconstructed from noise-free projections. The image on top is the ground truth image. The following rows are the CT reconstruction results using 75, 100 and 150 projections, respectively. Images from left to right in each row are the results obtained by FBP, SART with TV regularization, and the proposed robust wavelet frame based model (2.2), respectively.

ysis results for global reconstruction can be seen in Tables 3.1–3.3. It is shown that the SART method with the TV regularization and the proposed frame method (2.2) can remove more artifacts inside the region-of-interest (ROI) than the FBP method. For the FBP method, the artifacts make the final image much more difficult for diagnosis. For the SART+TV method, because of the lower approximation order of the TV regularization, it oversmoothes the reconstructed images. Therefore, compared to the proposed frame based method (2.2), its SSIM,
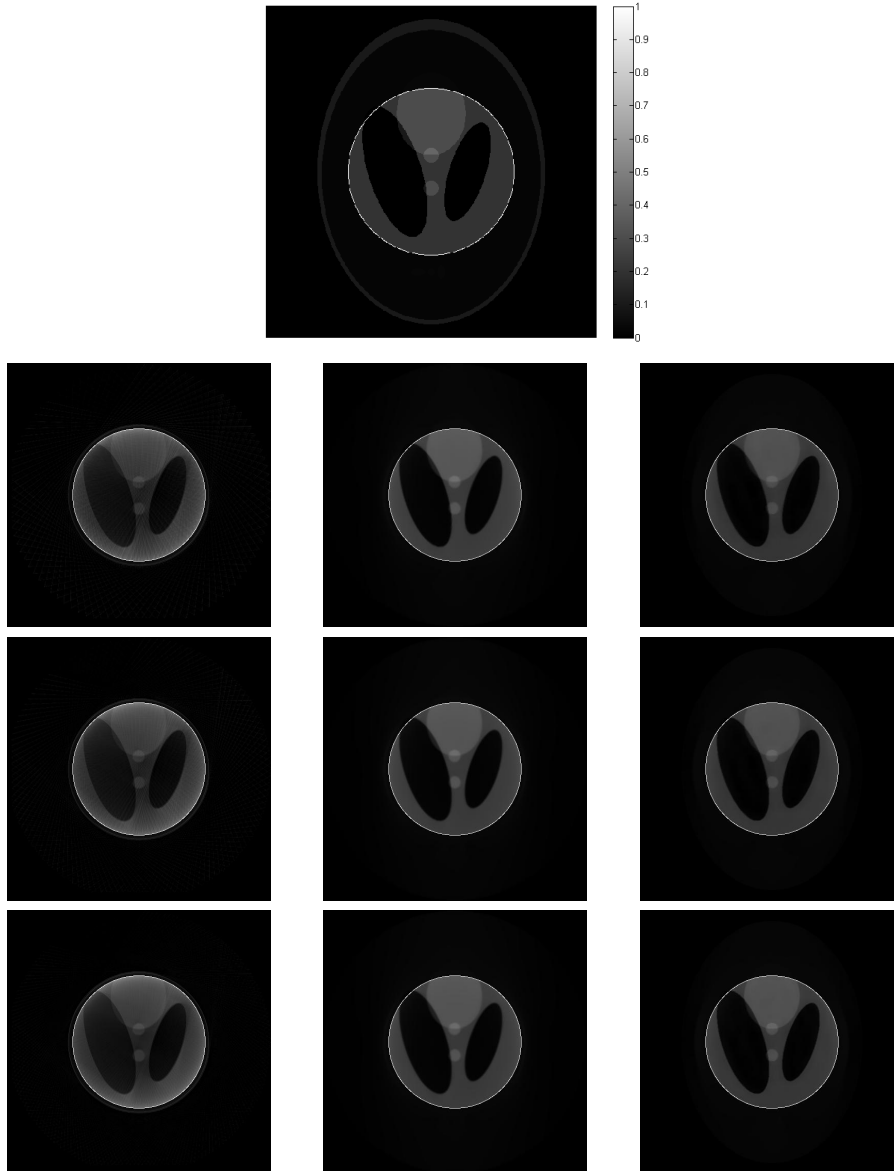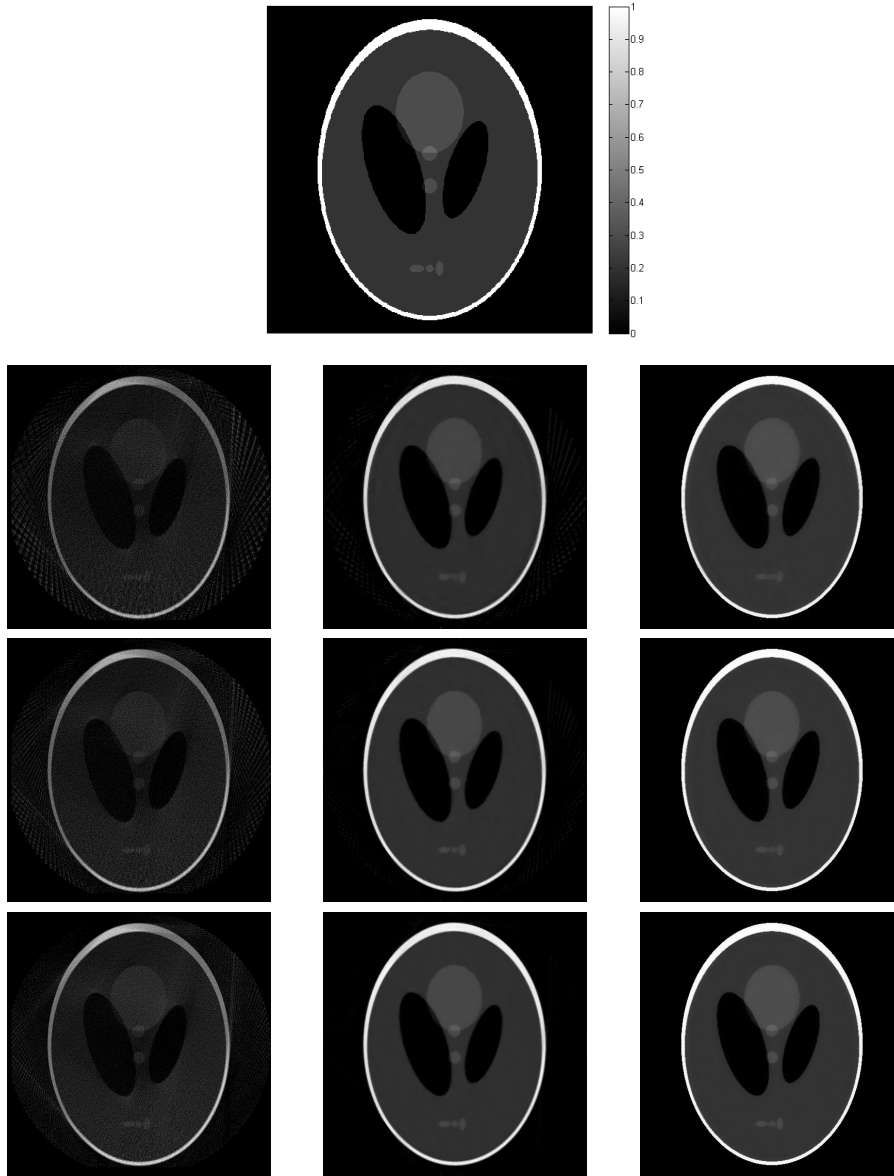
Fig. 3.3. The interior tomographic results (512 × 512) of the Shepp-Logan phantom reconstructed from noise-free projections. The image on top row is the ground truth image. The following rows are the CT reconstruction results using 75, 100 and 150 projections, respectively. Images from left to right in each row are the results obtained by FBP, SART with TV regularization, and the proposed robust wavelet frame based model (2.2), respectively. The highlighted parts in white circles centered at the middle of the phantom are the reconstructed ROI whose projection lines in all projection angles are available.

correlation, and CNR are smaller and the relative error is higher. In particular, Figs. 3.5 and 3.6 show that in the flat regions of ROI, the proposed method (2.2) has less standard deviation compared to the SART+TV method. It can also be shown in Fig. 3.7 that both the FBP method and the SART+TV oversmooth the sharp edges while the proposed robust method (2.2) can preserve such sharp edges. Consequently, the proposed robust frame based method

(2.2) has lowest relative error and highest correlation and CNR values since the frame based method with isotropic wavelet frame regularization can remove most of the artifacts in all direction and protect the sharp edges. Fig. 3.11 demonstrates the separation of the three systems and Fig. 3.12 shows that the three-system method has less error than the single-system method without a and n. Additionally, from Tables 3.2 and 3.3, it can be seen that the proposed frame based method (2.2) is most insensitive to noise.

Fig. 3.4. The tomographic results (512×512) of the Shepp-Logan phantom reconstructed from noisy projections with Poisson noise. The image on top is the ground truth image. The following rows are the CT reconstruction results using 75, 100 and 150 projections, respectively. Images from left to right in each row are the results obtained by FBP, SART with TV regularization, and the proposed robust wavelet frame based model (2.2), respectively.
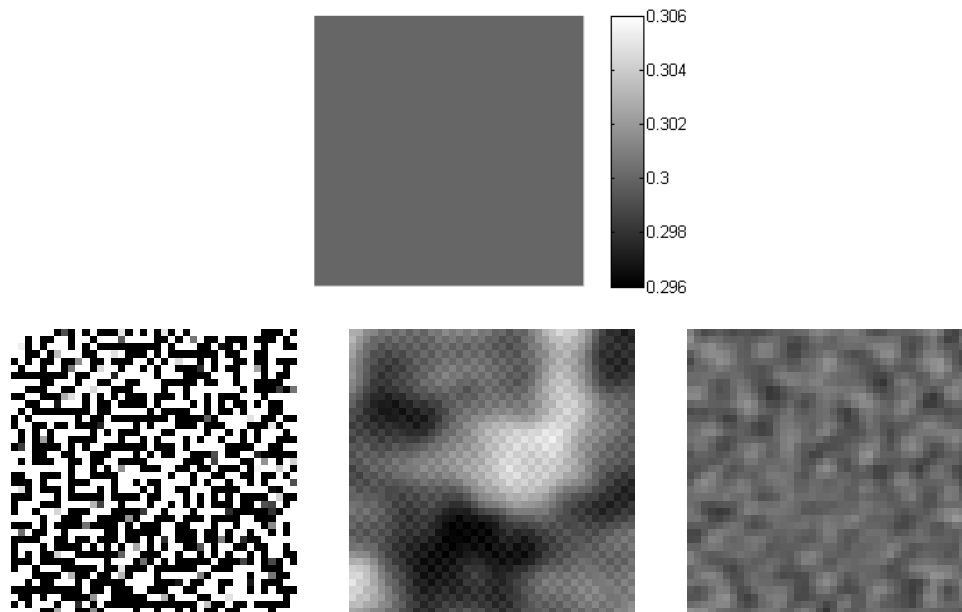
Fig. 3.5. *Zoom in images of a flat region of Fig. 3.4 for 150 projections. The region is indicated in Fig. 3.1. The image on top row is the ground truth image. For the bottom row, the images from left to right are the zoom in images obtained by FBP, SART with TV regularization, and robust wavelet frame based model (2.2), respectively.*
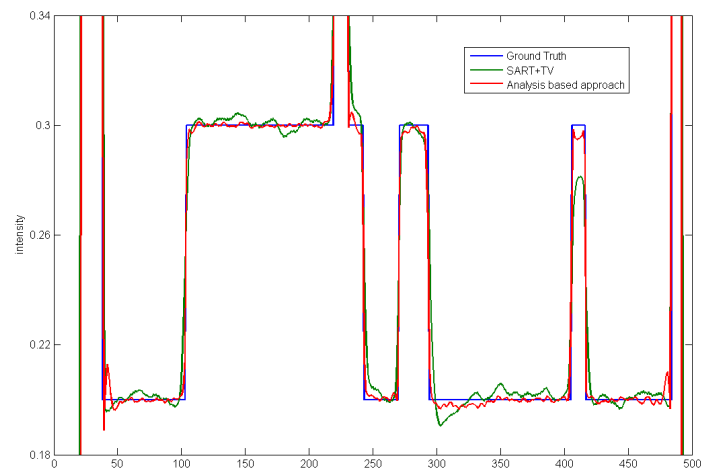

Fig. 3.6. *Representative of the profiles of the green line in the images in Fig. 3.1 reconstructed from 150 projections.*
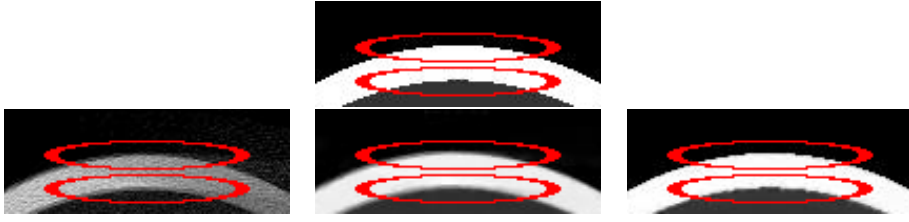
Fig. 3.7. Zoom in images of the edge parts of Fig. 3.4 for 150 projections. The image on top row is the zoom in part of assumed ground truth image with the color bar which is also shared for the bottom three images. For the bottom row, images from left to right are the zoom in images obtained by FBP, SART with TV regularization, and the proposed wavelet frame based approach (2.2), respectively.

The performance of the proposed isotropic wavelet frame based method, especially for the real preclinical sheep lung with complicated image structure, demonstrates the feasibility of applying wavelet frame based method to clinical applications. Furthermore, with the robustness of proposed wavelet frame based CT image reconstruction model, it is possible to reduce the radiation dose even if the projection matrix P suffers from mismatch.

Table 3.1: Comparison of mean SSIM (Gaussian window of size 11 and standard deviation 1.5), relative error, correlation and contrast-noise-ratio (CNR) for the reconstructed results of the Shepp-Logan phantom from noise-free projections.

N_p	FBP method				SART+TV method				Robust method (2.2)			
	SSIM	error	corr	CNR	SSIM	error	corr	CNR	SSIM	error	corr	CNR
75	0.832	0.516	0.927	520.7	0.952	0.219	0.969	1829.2	0.960	0.132	0.990	3097.5
100	0.856	0.470	0.931	629.7	0.953	0.216	0.970	1873.5	0.966	0.115	0.992	3494.2
150	0.882	0.436	0.934	738.4	0.953	0.216	0.970	1818.2	0.972	0.097	0.994	4021.4

Table 3.2: Comparison of mean SSIM (Gaussian window of size 11 and standard deviation 1.5), relative error, correlation and contrast-noise-ratio (CNR) for the reconstructed results of the Shepp-Logan phantom from projections with Poisson noise.

N_p	FBP method				SART+TV method				Robust method (2.2)			
	SSIM	error	corr	CNR	SSIM	error	corr	CNR	SSIM	error	corr	CNR
75	0.623	0.582	0.865	509.4	0.946	0.246	0.969	1506.2	0.959	0.135	0.989	3015.4
100	0.637	0.548	0.883	569.8	0.949	0.268	0.969	1661.8	0.964	0.115	0.991	3389.0
150	0.658	0.500	0.899	651.4	0.950	0.267	0.969	1681.0	0.970	0.101	0.994	3938.1

Table 3.3: Comparison of mean SSIM (Gaussian window of size 11 and standard deviation 1.5), relative error, correlation and contrast-noise-ratio (CNR) for the reconstructed results of the preclinical sheep lung.

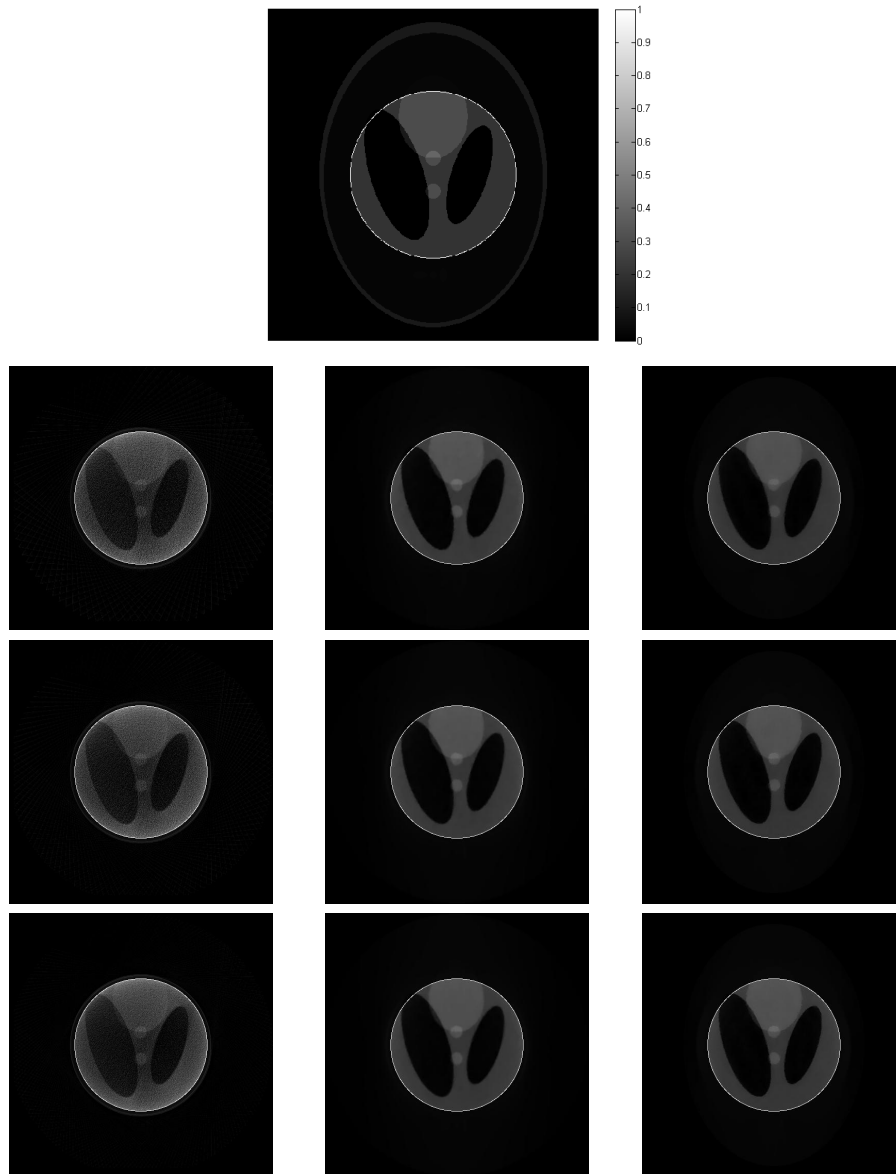| N_p	FBP method				SART+TV method				Robust method (2.2)			
	SSIM	error	corr	CNR	SSIM	error	corr	CNR	SSIM	error	corr	CNR
100	0.651	0.250	0.942	696.9	0.712	0.308	0.923	615.2	0.873	0.077	0.994	2332.3
150	0.709	0.262	0.954	787.4	0.727	0.264	0.932	639.9	0.899	0.061	0.996	2870.9
200	0.747	0.209	0.959	848.1	0.730	0.255	0.936	640.6	0.909	0.055	0.997	3136.9

Fig. 3.8. The interior tomographic results (512×512) of the Shepp-Logan phantom reconstructed from noisy projections with Poisson noise. The image on top row is the ground truth image. The following rows are the CT reconstruction results using 75, 100 and 150 projections, respectively. Images from left to right in each row are the results obtained by FBP, SART with TV regularization and robust wavelet frame based model (2.2), respectively. The highlighted parts in white circles centered at the middle of the phantom are the reconstructed ROI whose projection lines in all projection angles are available.
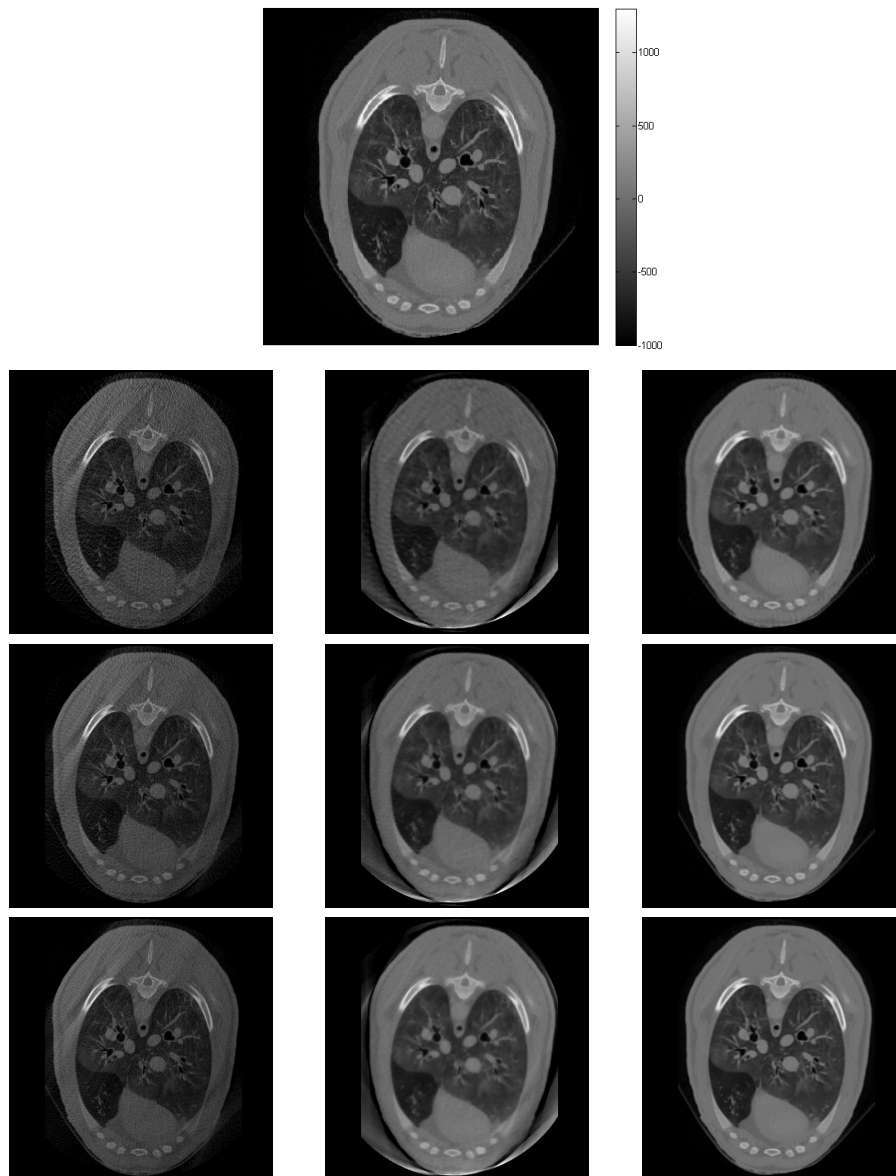
Fig. 3.9. The tomographic results (512 × 512) of the real sheep lung. The image on top row is the ground truth image and the corresponding greymap bar (Hounsfield Unit). The following rows are the CT reconstruction results using 100, 150 and 200 projections, respectively. Images from left to right in each row are the results obtained by FBP, SART with TV regularization, and robust wavelet frame based model (2.2), respectively.
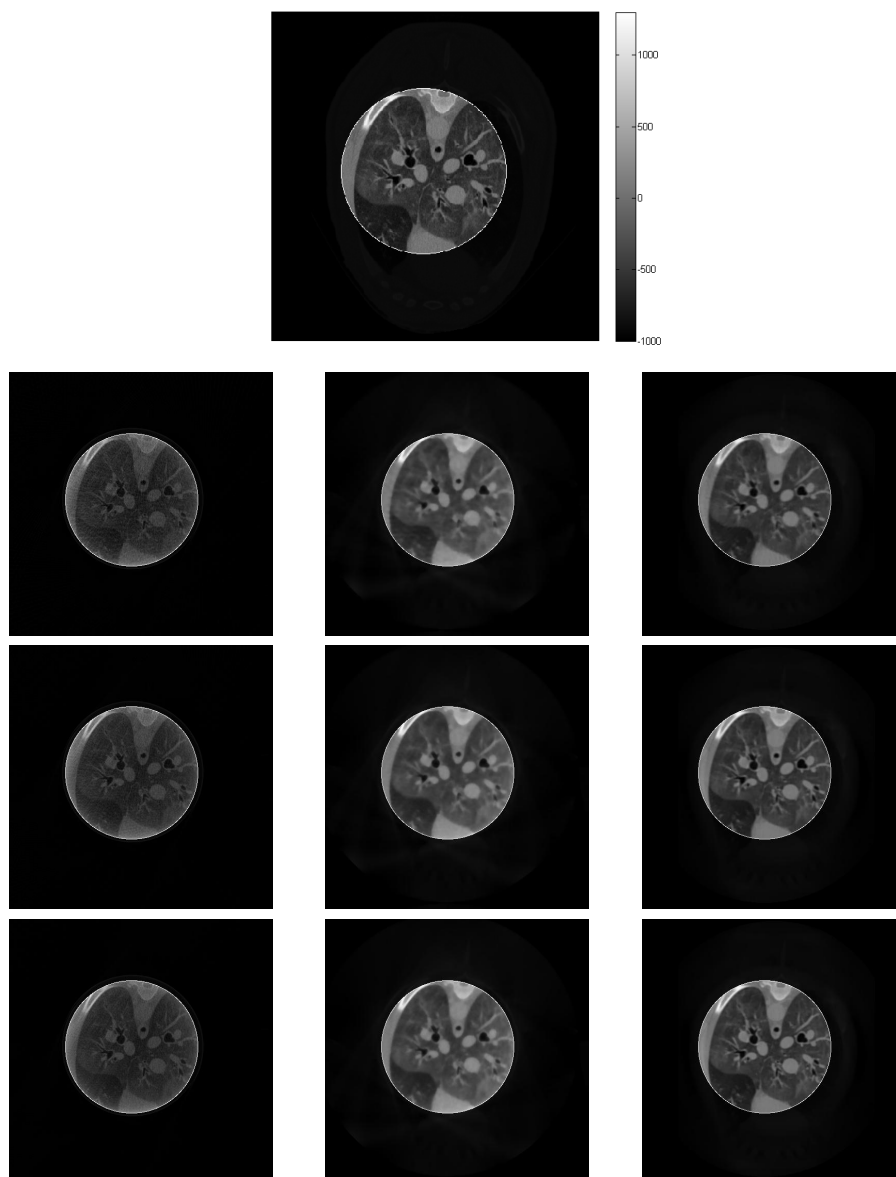
Fig. 3.10. The interior tomographic results (512 × 512) of the real sheep lung. The image on top row is the ground truth image and the corresponding greymap bar (Hounsfield Unit). The following rows are the CT reconstruction results using 100, 150 and 200 projections, respectively. Images from left to right in each row are the results obtained by FBP, SART with TV regularization, and the proposed robust wavelet frame based model (2.2), respectively. The highlighted parts in white circles centered at the middle of the phantom are the reconstructed ROI.
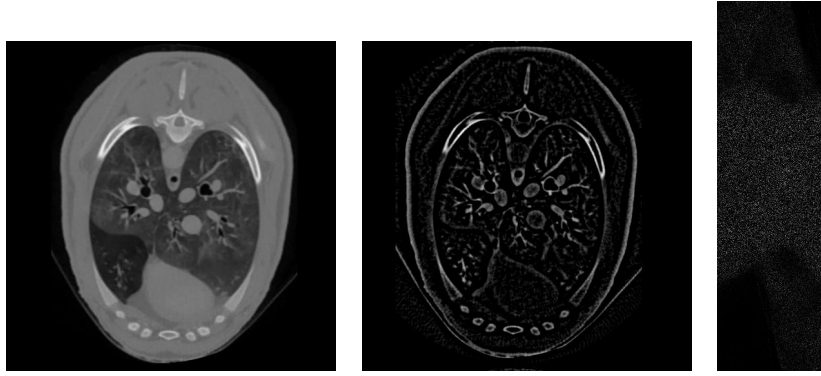
Fig. 3.11. The separation of three parts of the image for real sheep lung reconstruction from 200 projections through the proposed frame based approach (2.2). The images from left to right are the image part, artifacts part and the noise part in the Radon domain.
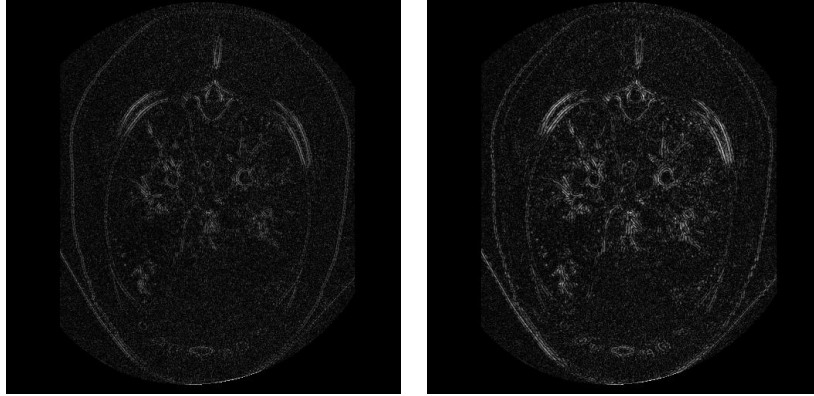

Fig. 3.12. The error for the CT reconstruction of the sheep lung from 200 projections. The left image is the error of the proposed three-system method (2.2) and the relative difference is 0.055. The right image is the error and single-system method $\min_u \quad \frac{1}{2}\|Pu - f\|_2^2 + \lambda_1 \|Wu\|_{1,2}$ and the relative difference becomes 0.069.

Due to the high intensity of some metal materials in clinical or industrial applications, the X-ray can not pass through certain region. As a result, all the projections involved in this region can not be measured, and the corresponding reconstruction problem for the rest of this region is called exterior tomography. In the last of this paper, we will show that the proposed method is also applied for exterior tomography. The exterior tomography results are shown in Fig. 3.13, from which it can be clearly observed that the FBP method is not applicable for exterior tomography while the rest two methods have better performance. In particular, the proposed frame based method (2.2) has apparently better visual quality in the exterior region. Furthermore, our proposed method (2.2) can estimate the intensity in some parts of the interior region while the other two methods cannot.
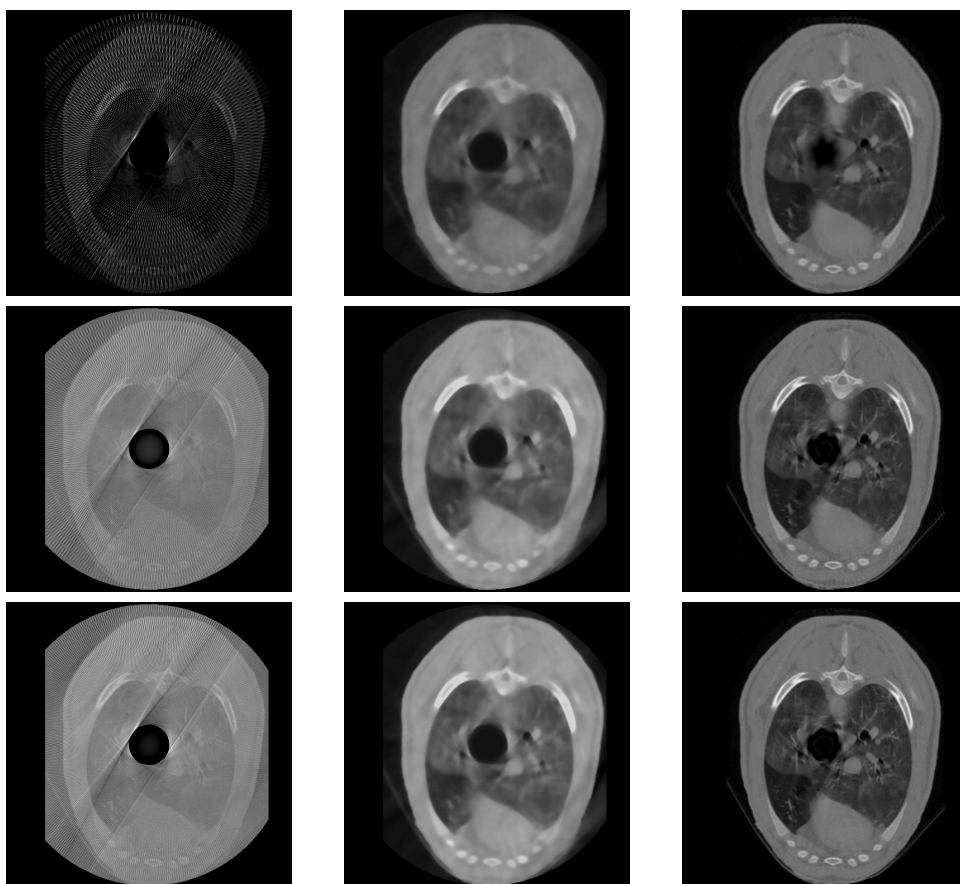
Fig. 3.13. The exterior tomographic results (512 × 512) of the real sheep lung. From the top to bottom, the CT images in each row are reconstructed from 100, 150 and 200 projections, respectively. Images from left to right are reconstructed by the FBP, SART with TV regularization, and the proposed robust wavelet frame based model (2.2), respectively.

4. Discussions and Conclusions

In this paper, we proposed a robust CT reconstruction model (2.2), which are based on the previous wavelet frame based models [13, 22], especially the analysis based approach [13]. The proposed robust CT reconstruction model introduces the three-system structure of the restored images and adds two regularization terms to treat the problem that P may mismatch the real measurements during the CT scan process. Fast algorithm is also developed by applying the split Bregman algorithm. Both numerical simulation and preclinical application were performed to evaluate the proposed algorithm. The results show that the proposed multi-system model outperforms the FBP and SART+TV methods in terms of the preservation of sharp edges, mean SSIM, contrast-to-noise ratio, relative error and correlations. Additionally, Figs. 3.3, 3.8 and 3.10 show that the proposed wavelet frame based method is applicable for interior tomography.

To be honest, we should admit that this paper has the limitations of the very rudimentary image quality (IQ) analysis. For example, the CNR value is just measure of magnitude of pixel standard deviation in a specific region. The other numerical results, such as relative error,

correlation and mean structural similarity, are mainly error based evaluations merely in the spatial domain. In the near future, a comprehensive evaluation is necessary to optimize the proposed algorithm, which may includes but not limited to the Fourier space analysis (MTF and NPS), numerical observer, and human observer studies. Moreover, to generalize the proposed model to a feasible polyenergetic X-ray model or scattering model, is also an important direction for the future work.

References

[1] J. Cai, R. Chan, and Z. Shen, *Simultaneous cartoon and texture inpainting*, Inverse Probl. Imaging (to appear), **4** (2010), 379–395.

[2] J. Cai, B. Dong, S. Osher, and Z. Shen, Image restorations: total variation, wavelet frames and beyond, *Journal of the American Mathematical Society*, **25**:4 (2012), 1033–1089.

[3] J. Cai, S. Osher, and Z. Shen, Linearized Bregman iterations for frame-based image deblurring, *SIAM J. Imaging Sci*, **2** (2009), 226–252.

[4] J. Cai, S. Osher, and Z. Shen, Split Bregman methods and frame based image restoration, *Multiscale Modeling and Simulation: A SIAM Interdisciplinary Journal*, **8** (2009), 337–369.

[5] A. Chambolle, An algorithm for total variation minimization and applications, *Journal of Mathematical Imaging and Vision*, **20** (2004), 89–97.

[6] R. Chan, T. Chan, L. Shen, and Z. Shen, Wavelet algorithms for high-resolution image reconstruction, *SIAM Journal on Scientific Computing*, **24** (2003), 1408–1432.

[7] R. H. Chan, S. D. Riemenschneider, L. Shen, and Z. Shen, Tight frame: an efficient way for high-resolution image reconstruction, *Applied and Computational Harmonic Analysis*, **17** (2004), 91–115.

[8] R. H. Chan, L. Shen, and Z. Shen, A framelet-based approach for image inpainting, *Research Report*, **4** (2005), 325.

[9] I. Daubechies, Ten lectures on wavelets, vol. CBMS-NSF Lecture Notes, SIAM, nr. 61, Society for Industrial Mathematics, 1992.

[10] I. Daubechies, B. Han, A. Ron, and Z. Shen, Framelets: Mra-based constructions of wavelet frames, *Applied and Computational Harmonic Analysis*, **14** (2003), 1–46.

[11] M. Defrise and R. Clack, A cone-beam reconstruction algorithm using shift-variant filtering and cone-beam backprojection, *IEEE Transactions on Medical Imaging*, **13** (1994), 186–195.

[12] B. Dong, H. Ji, J. Li, Z. Shen, and Y. Xu, Wavelet frame based blind image inpainting, *Applied and Computational Harmonic Analysis*, **32** (2012), 268–279.

[13] B. Dong, J. Li, and Z. Shen, X-ray ct image reconstruction via wavelet frame based regularization and radon domain inpainting, *Journal of Scientific Computing*, **54** (2013), 333–349.

[14] B. Dong and Z. Shen, MRA Based Wavelet Frames and Applications, IAS Lecture Notes Series, Summer Program on "The Mathematics of Image Processing", Park City Mathematics Institute, (2010).

[15] M. Elad, J. L. Starck, P. Querre, and D. L. Donoho, Simultaneous cartoon and texture image inpainting using morphological component analysis (MCA), *Applied and Computational Harmonic Analysis*, **19** (2005), 340–358.

[16] L. Feldkamp, L. Davis, and J. Kress, Practical cone-beam algorithm, *J. Opt. Soc. Am. A*, **1** (1984), 612–619.

[17] G. Gilboa and S. Osher, Nonlocal operators with applications to image processing, *Multiscale Model Sim*, **7** (2008), 1005–1028.

[18] T. Goldstein and S. Osher, The split Bregman algorithm for L1 regularized problems, *SIAM Journal on Imaging Sciences*, **2** (2009), pp. 323–343.

[19] R. Gordon, R. Bender, and G. Herman, Algebraic Reconstruction Techniques (ART) for three-dimensional electron microscopy and X-ray photography, *Journal of theoretical Biology*, **29** (1970), 471–481.

[20] W. Han, H. Yu, and G. Wang, A general total variation minimization theorem for compressed sensing based interior tomography, International Journal of Biomedical Imaging, (Article ID: 125871, 3 pages, 2009).

[21] H. Ji and K. Wang, Robust image deconvolution with inaccurate blur kernels, *IEEE Transactions on Image Processing*, (2012).

[22] X. Jia, B. Dong, Y. Lou, and S. B. Jiang, GPU-based iterative cone-beam CT reconstruction using tight frame regularization, *Physics in Medicine and Biology*, *56* (2011), 3787–3807.

[23] X. Jia, Y. Lou, R. Li, W. Y. Song, and S. B. Jiang, GPU-based fast cone beam CT reconstruction from undersampled and noisy projection data via total variation, *Medical physics*, **37** (2010), 1757.

[24] L. Li, Z. Chen, Y. Xing, L. Zhang, K. Kang, and G. Wang, A general exact method for synthesizing parallel-beam projections from cone-beam projections via filtered backprojection, *Phys Med Biol*, **51** (2006), 5643–5654.

[25] F. Noo, C. Bernard, F. Litt, and P. Marchot, A comparison between filtered backprojection algorithm and direct algebraic method in fan beam ct, *Signal Process*, **51** (1996), 191–199.

[26] J. Radon, Über die Bestimmung von Funktionen durch ihre Integralwerte längs gewisser Mannigfaltigkeiten, *Berichte Sächsische Akademie der Wissenschaften*, **69** (1917), 262–267.

[27] A. Ron and Z. Shen, Affine Systems in $L_2(\mathbb{R}^d)$: The Analysis of the Analysis Operator, *Journal of Functional Analysis*, **148** (1997), 408–447.

[28] L. Rudin, S. Osher, and E. Fatemi, Nonlinear total variation based noise removal algorithms, *Phys. D*, **60** (1992), 259–268.

[29] Z. Shen, Wavelet frames and image restorations, Proceedings of the International Congress of Mathematicians, Hyderabad, India, (2010).

[30] E. Y. Sidky, C. M. Kao, and X. Pan, Accurate image reconstruction from few-views and limited-angle data in divergent-beam CT, *Journal of X-Ray Science and Technology*, **14** (2006), 119–139.

[31] E. Y. Sidky and X. Pan, Image reconstruction in circular cone-beam computed tomography by constrained, total-variation minimization, *Physics in medicine and biology*, **53** (2008), 4777.

[32] P. Tseng, Convergence of a block coordinate descent method for nondifferentiable minimization, *Journal of optimization theory and applications*, **109** (2001), 475–494.

[33] Y. Ye, H. Yu, Y. Wei, and G. Wang, A general local reconstruction approach based on a truncated hilbert transform, International Journal of Biomedical Imaging, (Article ID: 63634, 8 pages, 2007).

[34] H. Yu and G. Wang, Compressed sensing based interior tomography, *Physics in Medicine and Biology*, **54**:9 (2009), 2791–2805.

[35] H. Yu, J. Yang, M. Jiang, and G. Wang, Supplemental analysis on compressed sensing based interior tomography, *Physics in Medicine and Biology*, **54**:18 (2009), N425–N432.

[36] H. Yu, Y. Ye, S. Zhao, and G. Wang, Local roi reconstruction via generalized fbp and bpf algorithms along more flexible curves, *International Journal of Biomedical Imaging*, (2006), 1–7.

[37] H. Yu, S. Zhao, A. Hoffman, and G. Wang, Ultra-low dose lung ct perfusion regularized by a previous scan, *Academic Radiology*, **16**:3 (2009), 363–373.

[38] H. R. Sheikh, Z. Wang, A. C. Bovik and E. P. Simoncelli, Image quality assessment: From error visibility to structural similarity, *IEEE Transactions on Image Processing*, **13**:4 (2004), 600–612.

[39] X. Zhang, M. Burger, X. Bresson, and S. Osher, Bregmanized nonlocal regularization for deconvolution and sparse reconstruction, *SIAM Journal on Imaging Sciences*, **3** (2010), 253–576.